



Review

Development of a broadband Mueller matrix ellipsometer as a powerful tool for nanostructure metrology



Shiyuan Liu^{*}, Xiuguo Chen, Chuanwei Zhang

State Key Laboratory of Digital Manufacturing Equipment and Technology, Huazhong University of Science and Technology, Wuhan, Hubei 430074, China

ARTICLE INFO

Available online 10 February 2015

Keywords:

Mueller matrix ellipsometry
 Mueller matrix polarimetry
 Depolarization
 Optical scatterometry
 Computational metrology
 Optical metrology
 Nanometrology
 Nanostructure

ABSTRACT

Ellipsometric scatterometry has gained wide industrial applications in semiconductor manufacturing after ten years of development. Among the various types of ellipsometers, Mueller matrix ellipsometer (MME) can provide all 16 elements of the 4 by 4 Mueller matrix, and consequently, MME-based scatterometry can acquire much more useful information about the sample and thereby can achieve better measurement sensitivity and accuracy. In this paper, the basic principles and instrumentation of MME are presented, and the data analysis in MME-based nanostructure metrology is revisited from the viewpoint of computational metrology. It is pointed out that MME-based nanometrology is essentially a computational metrology technique by modeling a complicated forward process followed by solving a nonlinear inverse problem. Several case studies are finally provided to demonstrate the potential of MME in nanostructure metrology.

© 2015 Elsevier B.V. All rights reserved.

Contents

1. Introduction	176
2. Fundamentals.	177
2.1. Basic principles and instrumentation of MME	177
2.2. Data analysis revisited from the viewpoint of computational metrology	178
3. Application to nanostructure metrology	180
3.1. Measurement of e-beam patterned grating structures	181
3.2. Measurement of nanoimprinted resist patterns	182
3.3. Measurement of lithographic patterns with line edge roughness	183
3.4. Measurement of etched trench nanostructures	184
4. Conclusions.	184
Acknowledgments	184
References.	184

1. Introduction

Nanomanufacturing is referred to as the manufacturing of products with feature dimensions at the nanometer scale. It is an essential bridge between the newest discoveries of fundamental nanoscience and real-world products by nanotechnology. One critical challenge to the

realization of nanomanufacturing is the development of necessary instrumentation and metrology at the nano-scale, especially the fast, low-cost, and non-destructive metrology techniques that are suitable in high-volume nanomanufacturing [1]. Although scanning electron microscopy (SEM), atomic force microscopy (AFM), or transmission electron microscopy (TEM) can provide high precision data, they are, in general, time-consuming, expensive, complex to operate, and problematic in realizing in-line integrated measurement.

Ellipsometry is an optical metrology technique that utilizes polarized light to characterize thickness of thin films and optical constants of both layered and bulk materials [2]. Since the year of around 2000,

^{*} Corresponding author at: State Key Laboratory of Digital Manufacturing Equipment and Technology, Huazhong University of Science and Technology, 1037 Luoyu Road, Wuhan, Hubei 430074, China. Tel.: +86 27 8755 9543; fax: +86 27 8755 8045.
 E-mail address: shyliu@hust.edu.cn (S. Liu).

spectroscopic ellipsometry (SE) was introduced to monitor the critical dimension (CD) of grating structures in semiconductor manufacturing [3–5]. Compared with SEM, AFM, and TEM, this technique, also referred to as optical scatterometry or optical critical dimension metrology, has achieved wide industrial applications after ten years of development due to its attractive advantages, such as low cost, high throughput, and minimal sample damage [6,7].

The application of ellipsometry for nanostructure metrology heavily relies on two key issues [8], i.e., the collection of a precise measured signature of a diffractive nanostructure as well as the fast and accurate reconstruction of the structural profile from the measured signature. The reconstruction of the structural profile from the measured signature is a typical inverse diffraction problem with an objective of finding a profile whose theoretical signature can best match the measured one. The solution of the inverse problem usually employs two kinds of methods [9], namely the nonlinear regression method [10,11] and the library search method [12–14]. Both of these two approaches involve the establishment of a theoretical diffraction model that relates the optical signatures and the structural profiles associated with these signatures. Many methods have been proposed to solve this diffraction model [15], of which the rigorous-coupled wave analysis (RCWA) [16–18] is the most common approach in optical scatterometry. The collection of the measured signature involves the development of a specific ellipsometer. Among the various types of ellipsometers, Mueller matrix ellipsometer (MME), also known as Mueller matrix polarimeter, can provide all 16 elements of the 4×4 Mueller matrix in each measurement. Compared with conventional ellipsometric scatterometry, which at most obtains two ellipsometric angles, MME-based scatterometry can acquire much more useful information about the sample, such as anisotropy and depolarization. Therefore, MME is expected to be a powerful tool for nanostructure metrology in high-volume nanomanufacturing.

Several researchers have investigated the MME-based nanostructure metrology over the past years [19–25]. Novikova et al. implemented MME in different azimuthal angles to characterize one-dimensional diffraction gratings [19,20]. It was shown that the Mueller matrices measured in proper conical diffraction configurations may help decouple some of the fitting parameters. We further proposed a measurement configuration optimization method for MME to find an optimal combination of the incidence and azimuthal angles, with which more accurate measurement can be achieved [21]. Kim and Li et al. investigated the possibility of measuring overlay and grating asymmetry with MME [22, 23]. Their research indicated that MME had good sensitivity to both the magnitude and direction of overlay and profile asymmetry, while conventional ellipsometric scatterometry had difficulty in distinguishing the direction of the above features. In our recent work, noticeable depolarization effects were observed from the measured Mueller matrices of nanoimprinted resist patterns [24,25]. We found that improved accuracy can be achieved for the line width, line height, sidewall angle, and residual layer thickness measurement after taking depolarization effects into account.

In this paper, we will review the principles and potential of MME in nanostructure metrology to provide a complete picture of this technique. We will first introduce the basic principles and instrumentation of MME, with a demonstration of the development of a broadband dual rotating-compensator Mueller matrix ellipsometer in our lab. Then we will revisit the data analysis in MME-based nanostructure metrology from the viewpoint of computational metrology [26,27], and point out that MME-based nanometrology is essentially a computational metrology technique by modeling a complicated forward process followed by solving a corresponding nonlinear inverse problem. Finally, we will present several case studies in MME-based nanostructure metrology, including the measurement of e-beam patterned grating structures, the measurement of nanoimprinted resist patterns, the measurement of lithographic patterns with line edge roughness (LER), and the measurement of etched trench nanostructures that are typically encountered in the manufacturing of flash memory

storage cells, to demonstrate the capability of MME in nanostructure metrology.

2. Fundamentals

2.1. Basic principles and instrumentation of MME

The measurement of Mueller matrix involves a series of K ($K \geq 16$) flux measurements made by illuminating the sample with different polarization states and analyzing the exiting beam with different analyzers. The k -th measured flux g_k is related to the sample Mueller matrix \mathbf{M} by [28]

$$g_k = \mathbf{A}_k^T \mathbf{M} \mathbf{S}_k = (\mathbf{S}_k \otimes \mathbf{A}_k)^T \mathbf{m}, \quad 1 \leq k \leq K, \quad (1)$$

where the symbol \otimes denotes the Kronecker product, the superscript “T” denotes the transpose, \mathbf{S}_k is the k -th incident polarization state produced by the polarization state generator (PSG), and \mathbf{A}_k is the k -th exiting polarization state produced by the polarization state analyzer (PSA). \mathbf{m} is a 16×1 Mueller vector obtained by reading the sample Mueller matrix elements in the lexicographic order, i.e., $\mathbf{m} = [M_{11}, M_{12}, M_{13}, M_{14}, M_{21}, M_{22}, \dots, M_{44}]^T$. Eq. (1) can be written in a matrix form as

$$\mathbf{G} = \mathbf{D} \mathbf{m}, \quad (2)$$

where \mathbf{G} is a $K \times 1$ column vector with the k -th element being g_k , and \mathbf{D} is a $K \times 16$ matrix with the k -th row vector being $(\mathbf{S}_k \otimes \mathbf{A}_k)^T$. According to Eq. (2), the sample Mueller matrix can be measured by

$$\mathbf{m} = \mathbf{D}^+ \mathbf{G}, \quad (3)$$

where $\mathbf{D}^+ = (\mathbf{D}^T \mathbf{D})^{-1} \mathbf{D}^T$ is the Moore–Penrose pseudo-inverse of matrix \mathbf{D} . Eq. (3) is the basic and general principle of sample Mueller matrix measurement for any type of Mueller matrix ellipsometers, such as the Mueller matrix ellipsometer based on the coupled ferroelectric liquid crystal cell [29,30], the dual rotating-compensator [31,32], or the four photoelastic modulators [33]. The dual rotating-compensator configuration was adopted in the development of the Mueller matrix ellipsometer in our lab.

Specifically, as schematically shown in Fig. 1, the basic system layout of the dual rotating-compensator Mueller matrix ellipsometer in order of light propagation is $\text{PC}_{r1}(\omega_1) \text{SC}_{r2}(\omega_2) \text{A}$, where P and A stand for the polarizer and analyzer, C_{r1} and C_{r2} refer to the 1st and 2nd rotating compensators, and S stands for the sample. The fast axis angles C_1 and C_2 of the 1st and 2nd compensators rotate synchronously at $\omega_1 = 5\omega$ and $\omega_2 = 3\omega$, where ω is the fundamental mechanical frequency. The Stokes vector \mathbf{S}_{out} of the exiting light beam can be expressed as the following Mueller matrix product [25,32]

$$\mathbf{S}_{\text{out}} = [\mathbf{M}_A \mathbf{R}(A)] [\mathbf{R}(-C_2) \mathbf{M}_{C_2}(\delta_2) \mathbf{R}(C_2)] [\mathbf{M} \mathbf{R}(-C_1) \mathbf{M}_{C_1}(\delta_1) \mathbf{R}(C_1)] [(-P) \mathbf{M}_P \mathbf{R}(P)] \mathbf{S}_{\text{in}}, \quad (4)$$

where \mathbf{M}_i ($i = P, A, C_1, C_2$) is the Mueller matrix associated with each optical element. $\mathbf{R}(\alpha)$ is the Mueller rotation transformation matrix for rotation by the angle α [$\alpha = P, A, C_1$, and C_2] that describes the corresponding orientation angle of each optical element. δ_1 and δ_2 are the wavelength-dependent phase retardances of the 1st and 2nd rotating compensators. By multiplying the matrices in Eq. (4), we can obtain the following expression for the irradiance at the detector (proportional to the first element of \mathbf{S}_{out}) [32]

$$I(t) = I_{00} M_{11} \left\{ a_0 + \sum_{n=1}^{16} [a_{2n} \cos(2n\omega t - \phi_{2n}) + b_{2n} \sin(2n\omega t - \phi_{2n})] \right\} \\ = I_0 \left\{ 1 + \sum_{n=1}^{16} [\alpha_{2n} \cos(2n\omega t - \phi_{2n}) + \beta_{2n} \sin(2n\omega t - \phi_{2n})] \right\}, \quad (5)$$

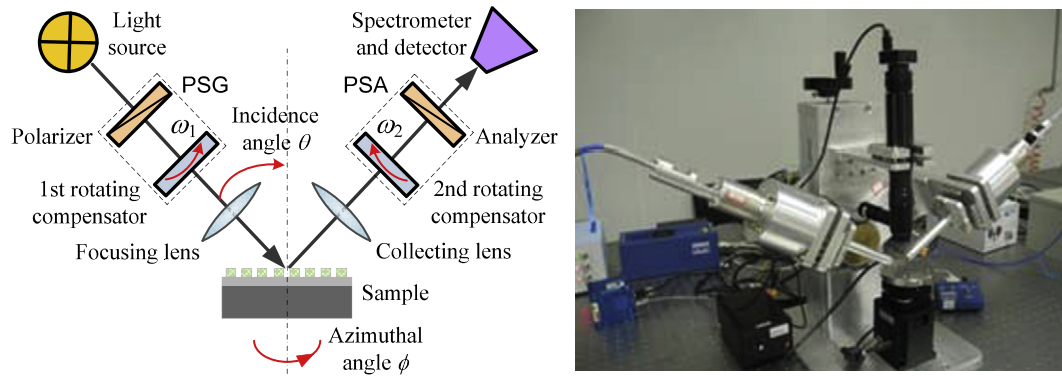


Fig. 1. Principle and prototype of the dual rotating-compensator Mueller matrix ellipsometer.

where I_{00} is the spectral response function and ϕ_{2n} is the angular phase shift. $I_0 = I_{00}M_{11}a_0$, $\alpha_{2n} = a_{2n}/a_0$, and $\beta_{2n} = b_{2n}/a_0$ are the d.c. and d.c.-normalized a.c. harmonic coefficients, respectively. The sample Mueller matrix elements M_{ij} ($i, j = 1, 2, 3, 4$) are linear combinations of α_{2n} and β_{2n} . By performing Fourier analysis [34], the sample Mueller matrix elements can be extracted from these harmonic coefficients. Based on the above measurement principle, we developed a Mueller matrix ellipsometer prototype, as depicted in Fig. 1. Currently, the spectral range is from 200 to 1000 nm. The beam diameter can be changed from the nominal value of ~ 3 mm to a value of ~ 200 μm equipped with the focusing lens. The two arms of the ellipsometer and the sample stage can be rotated to change the incidence and azimuthal angles in experiments.

2.2. Data analysis revisited from the viewpoint of computational metrology

In the MME-based nanostructure metrology, the optical signature, i.e., the Mueller matrix spectra, of the nanostructure is measured and then an optical model corresponding to the nanostructure is constructed. The next step is the parameter extraction, which involves an inverse diffraction problem solving. In this step, the calculated signature from the constructed optical model is adjusted iteratively to find a signature that can best match the measured one. The structural parameters associated with the calculated best-fit signature will be treated as the final measurement results.

The MME-based nanostructure metrology is essentially a model-based technique and heavily depends on two key techniques, i.e., the forward optical modeling and the inverse parameter extraction, which are both computationally intensive. Recently, we termed such kind of

model-based metrology as *computational metrology* [26,27], with an emphasis on solving the vast and complicated scientific computations, especially numerical computations. In general terms *computational metrology* can be defined as the measurement where a complicated measurement process is modeled as a forward problem, and the measured data are collected by a specific instrument under a certain measurement configuration, and then the measurands are precisely and accurately extracted from the measured data by solving the corresponding inverse problem. The fundamental principles of computational metrology are summarized as shown in Fig. 2, whose basic elements include the measurands, measurement configuration, forward model, measured data, and solution of measurands. The rest of this section will review the data analysis in MME-based nanostructure metrology from the viewpoint of computational metrology.

Without loss of generality, we denote the measurands as a P -dimensional vector $\mathbf{x} = [x_1, x_2, \dots, x_P]^T$, where x_1, x_2, \dots, x_P can be the line width, line height, and sidewall angle of the grating sample under measurement. The measurement configuration is defined as the combination of selected wavelengths λ , incidence angles θ , and azimuthal angles ϕ , and is represented by $\mathbf{a} = [\lambda, \theta, \phi]^T$. The optical signature of the grating sample can be calculated by rigorous coupled-wave analysis (RCWA) [16–18]. In RCWA, both the permittivity function and electromagnetic field components are expanded into Fourier series. Afterwards, the tangential field components are matched at boundaries between different layers, and thereby the boundary-value problem is reduced to an algebraic eigenvalue problem. Consequently, the overall reflection coefficients can be calculated by solving the eigenvalue problem. According to the reflection coefficients, the 2×2 Jones matrix $\mathbf{J}(\mathbf{x}, \mathbf{a})$ associated with the zeroth-order diffracted light of the

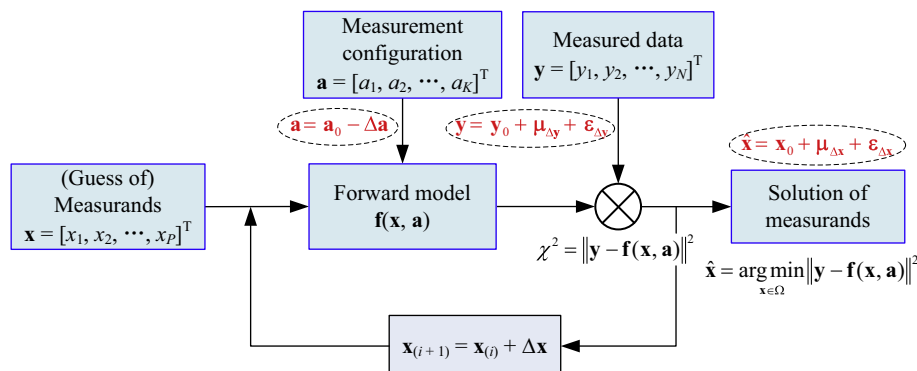


Fig. 2. Fundamental principles and basic elements of computational metrology.

sample, which connects the incoming Jones vector with the diffracted one, can be formulated by

$$\begin{bmatrix} E_{rp} \\ E_{rs} \end{bmatrix} = \mathbf{J}(\mathbf{x}, \mathbf{a}) \begin{bmatrix} E_{ip} \\ E_{is} \end{bmatrix} = \begin{bmatrix} r_{pp} & r_{ps} \\ r_{sp} & r_{ss} \end{bmatrix} \begin{bmatrix} E_{ip} \\ E_{is} \end{bmatrix}, \quad (6)$$

where $E_{s,p}$ refers to the electric field component perpendicular and parallel to the plane of incidence, respectively. If the sample is non-depolarizing, the 4×4 Mueller matrix $\mathbf{M}(\mathbf{x}, \mathbf{a})$ can be calculated from the Jones matrix $\mathbf{J}(\mathbf{x}, \mathbf{a})$ by [2]

$$\mathbf{M}(\mathbf{x}, \mathbf{a}) = \begin{bmatrix} M_{11} & M_{12} & M_{13} & M_{14} \\ M_{21} & M_{22} & M_{23} & M_{24} \\ M_{31} & M_{32} & M_{33} & M_{34} \\ M_{41} & M_{42} & M_{43} & M_{44} \end{bmatrix} = \mathbf{A}[\mathbf{J}(\mathbf{x}, \mathbf{a}) \otimes \mathbf{J}^*(\mathbf{x}, \mathbf{a})] \mathbf{A}^{-1}, \quad (7a)$$

where $\mathbf{J}^*(\mathbf{x}, \mathbf{a})$ is the complex conjugate of $\mathbf{J}(\mathbf{x}, \mathbf{a})$, and the matrix \mathbf{A} is given by

$$\mathbf{A} = \begin{bmatrix} 1 & 0 & 0 & 1 \\ 1 & 0 & 0 & -1 \\ 0 & 1 & 1 & 0 \\ 0 & i & -i & 0 \end{bmatrix}. \quad (7b)$$

In practice, the Mueller matrix $\mathbf{M}(\mathbf{x}, \mathbf{a})$ is usually normalized to the (1, 1)th element M_{11} , with the normalized Mueller matrix elements $m_{ij} = M_{ij}/M_{11}$.

When the sample has a depolarization effect, totally polarized light used as a probe in ellipsometry is transformed into partially polarized light. In this case, the Mueller matrix is a depolarizing one. The depolarization effect of a depolarizing Mueller matrix can be characterized by the depolarization index DI defined by [35]

$$DI = \left[\frac{\text{Tr}(\mathbf{M}\mathbf{M}^T) - M_{11}^2}{3M_{11}^2} \right]^{1/2}, \quad 0 \leq DI \leq 1, \quad (8)$$

where $\text{Tr}(\cdot)$ represents the matrix trace. $DI = 0$ and $DI = 1$ correspond to the totally depolarizing and non-depolarizing Mueller matrices, respectively. Many factors may induce depolarization effects in optical scatterometry [24,25], such as finite spectral bandwidth of the monochromator, finite numerical aperture (NA) of focusing lens in the measurement system, thickness nonuniformity in a thin film formed on a substrate, incoherent superposition of the light from two or more materials, and large surface or edge roughness of a sample. In the analysis a depolarizing sample, Eqs. (7a) and (7b) cannot be applied to directly derive the Mueller matrix from the corresponding Jones matrix any more. The optical modeling principle is based on the optical equivalence of the polarization states [36], which states that a depolarizing system is optically equivalent to a system composed of a parallel combination of several non-depolarizing systems. We further deduce that a depolarizing Mueller matrix can be written as the sum of various non-depolarizing Mueller matrices, i.e., [25]

$$\mathbf{M}^D = \int \rho(\mathbf{u}) \mathbf{M}^{ND}(\mathbf{u}) d\mathbf{u}, \quad (9)$$

where \mathbf{M}^D and \mathbf{M}^{ND} represent the depolarizing and non-depolarizing Mueller matrices, respectively, and the latter can be calculated by Eqs. (7a) and (7b). The variables \mathbf{u} denotes the factors that induce depolarization, and $\rho(\mathbf{u})$ is a weighting function, which can be specifically the spectral bandwidth function, numerical aperture, or thickness distribution function.

A weighted least-squares regression analysis (Levenberg–Marquardt algorithm) [10,11] or library search [12–14] is then performed, during which the measurands are varied until the calculated and measured data match as much close as possible. The solution of measurands $\hat{\mathbf{x}}$ can be achieved by minimizing a weighted mean-square error function χ_r^2 defined by

$$\chi_r^2 = \frac{1}{15N_\lambda - P} \chi^2 = \frac{1}{15N_\lambda - P} \sum_{k=1}^{N_\lambda} \sum_{i,j=1}^4 \left[\frac{m_{ij,k}^{\text{meas}} - m_{ij,k}^{\text{calc}}(\mathbf{x}, \mathbf{a})}{\sigma(m_{ij,k})} \right]^2, \quad (10)$$

where k indicates the k -th spectral point from the total number N_λ , indices i and j show all the Mueller matrix elements except m_{11} , and P is the total number of measurands. $m_{ij,k}^{\text{meas}}$ denotes the measured Mueller matrix elements, and $m_{ij,k}^{\text{calc}}(\mathbf{x}, \mathbf{a})$ denotes the calculated Mueller matrix elements associated with the measurands \mathbf{x} and the measurement configuration \mathbf{a} . Since the wavelengths λ are varied in a spectral range, here the vector \mathbf{a} is only the combination of fixed incidence and azimuthal angles, i.e., $\mathbf{a} = [\theta, \phi]^T$. $\sigma(m_{ij,k})$ is the estimated standard deviation associated with $m_{ij,k}$.

In practice, the MME-based nanostructure metrology process invariably has errors. These errors, which can be generally categorized into random and systematic errors, have great influences on the final precision and accuracy of the solution of measurands. An objective of the computational metrology is to quantitatively determine the values of measurands [26,27]. It is therefore necessary to theoretically analyze the error propagation and estimation in MME-based nanostructure metrology. For clarity, the measured Mueller matrix elements $m_{ij,k}^{\text{meas}}$ in Eq. (10) are marked as y_n with the three indices i, j and k lumped into a single one n . The calculated Mueller matrix elements $m_{ij,k}^{\text{calc}}(\mathbf{x}, \mathbf{a})$ are correspondingly marked as $f_n(\mathbf{x}, \mathbf{a})$. Ignoring the constant coefficient in the front of Eq. (10), we have

$$\chi^2 = \sum_{n=1}^N w_n [y_n - f_n(\mathbf{x}, \mathbf{a})]^2 = [\mathbf{y} - \mathbf{f}(\mathbf{x}, \mathbf{a})]^T \mathbf{W} [\mathbf{y} - \mathbf{f}(\mathbf{x}, \mathbf{a})], \quad (11)$$

where \mathbf{W} is an $N \times N$ diagonal matrix with diagonal elements $w_n = 1/\sigma^2(y_n)$ and $N = 15N_\lambda$. The inverse problem in MME-based nanostructure metrology is then formulated as [13]

$$\hat{\mathbf{x}} = \arg \min_{\mathbf{x} \in \Omega} \{ [\mathbf{y} - \mathbf{f}(\mathbf{x}, \mathbf{a})]^T \mathbf{W} [\mathbf{y} - \mathbf{f}(\mathbf{x}, \mathbf{a})] \}. \quad (12)$$

We assume that the function $\mathbf{f}(\mathbf{x}, \mathbf{a})$ is sufficiently smooth and can be expanded in a Taylor series which, truncated to the first-order, leads to a linear model at $(\hat{\mathbf{x}}, \mathbf{a})$

$$\mathbf{f}(\mathbf{x}', \mathbf{a}') = \mathbf{f}(\hat{\mathbf{x}}, \mathbf{a}) + \mathbf{J}_x \cdot (\mathbf{x}' - \hat{\mathbf{x}}) + \mathbf{J}_a \cdot (\mathbf{a}' - \mathbf{a}), \quad (13)$$

where \mathbf{J}_x and \mathbf{J}_a are the $N \times P$ and $N \times 2$ Jacobian matrices with respect to \mathbf{x} and \mathbf{a} , respectively, whose elements are given by

$$[\mathbf{J}_x]_{ij} = \left. \frac{\partial f_i(\mathbf{x}', \mathbf{a}')}{\partial x_j} \right|_{\mathbf{x}' = \hat{\mathbf{x}}, \mathbf{a}' = \mathbf{a}}, \quad (14a)$$

$$[\mathbf{J}_a]_{ij} = \left. \frac{\partial f_i(\mathbf{x}', \mathbf{a}')}{\partial a_j} \right|_{\mathbf{x}' = \hat{\mathbf{x}}, \mathbf{a}' = \mathbf{a}}. \quad (14b)$$

Substitution of $\mathbf{x}' = \mathbf{x}_0$ and $\mathbf{a}' = \mathbf{a}_0$ into Eq. (13) gives

$$\mathbf{f}(\mathbf{x}_0, \mathbf{a}_0) = \mathbf{f}(\hat{\mathbf{x}}, \mathbf{a}) + \mathbf{J}_x \Delta \mathbf{x} + \mathbf{J}_a \Delta \mathbf{a}, \quad (15)$$

where \mathbf{x}_0 and \mathbf{a}_0 are the true values of \mathbf{x} and \mathbf{a} , respectively. $\Delta \mathbf{x}$ and $\Delta \mathbf{a}$ represent the error propagated into $\hat{\mathbf{x}}$ and the configuration error in parameter extraction, respectively, and are given by $\Delta \mathbf{x} = \mathbf{x}_0 - \hat{\mathbf{x}}$ and $\Delta \mathbf{a} = \mathbf{a}_0 - \mathbf{a}$. The measured data \mathbf{y} will be the sum of the true signature

$\mathbf{y}_0 = \mathbf{f}(\mathbf{x}_0, \mathbf{a}_0)$ of the sample, a deterministic offset vector $\boldsymbol{\mu}_{\Delta\mathbf{y}}$, and a random noise vector $\boldsymbol{\varepsilon}_{\Delta\mathbf{y}}$, i.e.,

$$\mathbf{y} = \mathbf{f}(\mathbf{x}_0, \mathbf{a}_0) + \boldsymbol{\mu}_{\Delta\mathbf{y}} + \boldsymbol{\varepsilon}_{\Delta\mathbf{y}}. \quad (16)$$

Inserting Eqs. (15) and (16) into Eq. (12), we have

$$\begin{aligned} \chi_{\min}^2 &= [\mathbf{y} - \mathbf{f}(\hat{\mathbf{x}}, \mathbf{a})]^T \mathbf{W} [\mathbf{y} - \mathbf{f}(\hat{\mathbf{x}}, \mathbf{a})] \\ &= [\mathbf{J}_x \Delta \mathbf{x} + \mathbf{J}_a \Delta \mathbf{a} + \boldsymbol{\mu}_{\Delta\mathbf{y}} + \boldsymbol{\varepsilon}_{\Delta\mathbf{y}}]^T \mathbf{W} [\mathbf{J}_x \Delta \mathbf{x} + \mathbf{J}_a \Delta \mathbf{a} + \boldsymbol{\mu}_{\Delta\mathbf{y}} + \boldsymbol{\varepsilon}_{\Delta\mathbf{y}}]. \end{aligned} \quad (17)$$

By taking the derivative of both sides of Eq. (17) with respect to \mathbf{x} , we derive [21,37]

$$\tilde{\mathbf{J}}_x \Delta \mathbf{x} + \tilde{\mathbf{J}}_a \Delta \mathbf{a} + \tilde{\boldsymbol{\mu}}_{\Delta\mathbf{y}} + \tilde{\boldsymbol{\varepsilon}}_{\Delta\mathbf{y}} = 0, \quad (18)$$

where $\tilde{\mathbf{J}}_x = \mathbf{W}^{1/2} \mathbf{J}_x$, $\tilde{\mathbf{J}}_a = \mathbf{W}^{1/2} \mathbf{J}_a$, $\tilde{\boldsymbol{\mu}}_{\Delta\mathbf{y}} = \mathbf{W}^{1/2} \boldsymbol{\mu}_{\Delta\mathbf{y}}$, and $\tilde{\boldsymbol{\varepsilon}}_{\Delta\mathbf{y}} = \mathbf{W}^{1/2} \boldsymbol{\varepsilon}_{\Delta\mathbf{y}}$. Eq. (18) relates the error $\Delta \mathbf{x}$ in $\hat{\mathbf{x}}$ with the error sources such as the configuration error $\Delta \mathbf{a}$ as well as the systematic and random errors $\boldsymbol{\mu}_{\Delta\mathbf{y}}$ and $\boldsymbol{\varepsilon}_{\Delta\mathbf{y}}$ in \mathbf{y} . Assuming the random noise vector $\boldsymbol{\varepsilon}_{\Delta\mathbf{y}}$ has a zero mean and $\varepsilon_{\Delta y_n} \sim \mathcal{N}(0, \sigma^2(y_n))$, we can derive the covariance matrix of $\hat{\mathbf{x}}$ that

$$\mathbf{C}(\hat{\mathbf{x}}) = \tilde{\mathbf{J}}_x^+ \cdot \mathbf{C}(\tilde{\boldsymbol{\varepsilon}}_{\Delta\mathbf{y}}) \cdot (\tilde{\mathbf{J}}_x^+)^T = (\tilde{\mathbf{J}}_x^T \tilde{\mathbf{J}}_x)^{-1}, \quad (19)$$

where $\tilde{\mathbf{J}}_x^+ = (\tilde{\mathbf{J}}_x^T \tilde{\mathbf{J}}_x)^{-1} \tilde{\mathbf{J}}_x^T$ is the Moore–Penrose pseudo-inverse of matrix $\tilde{\mathbf{J}}_x$. The standard deviation of parameter x_i ($i = 1, 2, \dots, P$) can be estimated from the diagonal elements of $\mathbf{C}(\hat{\mathbf{x}})$ and is given by

$$\sigma(x_i) = \sqrt{[\mathbf{C}(\hat{\mathbf{x}})]_{ii}}. \quad (20)$$

The estimated uncertainty in parameter x_i with a desired confidence level is then given by

$$u(x_i) = \kappa \sigma(x_i), \quad (21)$$

where κ is coverage factor associated with the prescribed confidence level. By taking the mean value of both sides of Eq. (18), we can derive

$$\boldsymbol{\mu}_{\Delta\mathbf{x}} = \langle \Delta \mathbf{x} \rangle = \tilde{\mathbf{J}}_x^+ \tilde{\mathbf{J}}_a \Delta \mathbf{a} + \tilde{\mathbf{J}}_x^+ \tilde{\boldsymbol{\mu}}_{\Delta\mathbf{y}}, \quad (22)$$

which describes how the configuration error $\Delta \mathbf{a}$ and the systematic error $\boldsymbol{\mu}_{\Delta\mathbf{y}}$ in \mathbf{y} lead to the systematic error $\boldsymbol{\mu}_{\Delta\mathbf{x}}$ in $\hat{\mathbf{x}}$. According to Eq. (22), we can estimate the systematic error $\boldsymbol{\mu}_{\Delta\mathbf{x}}$ in $\hat{\mathbf{x}}$ if we know the configuration error $\Delta \mathbf{a}$ and the systematic error $\boldsymbol{\mu}_{\Delta\mathbf{y}}$ in \mathbf{y} . However, in practice, the errors $\Delta \mathbf{a}$ and $\boldsymbol{\mu}_{\Delta\mathbf{y}}$ are usually difficult to obtain, which makes the above estimation unfeasible. As described in Eq. (22), the systematic error $\boldsymbol{\mu}_{\Delta\mathbf{x}}$ in $\hat{\mathbf{x}}$ will be mainly induced by the configuration error $\Delta \mathbf{a}$ if we assume the measurement system is well calibrated and the systematic error $\boldsymbol{\mu}_{\Delta\mathbf{y}}$ in \mathbf{y} is small. In this case, we can optimize the measurement configuration by [21,25]

$$(\theta_{\text{opt}}, \phi_{\text{opt}}) = \arg \min_{\theta \in \Theta, \phi \in \Phi} \left[\max_{\mathbf{x} \in \Omega} (\|\tilde{\mathbf{J}}_x^+ \tilde{\mathbf{J}}_a\|) \right], \quad (23)$$

to find an optimal combination of fixed incidence and azimuthal angles, with which more accurate measurement can be achieved. The notation $\|\cdot\|$ in Eq. (23) represents the ℓ_p ($p = 1, 2, \infty$) matrix norm.

3. Application to nanostructure metrology

Four kinds of nanostructures were measured using the in-house developed Mueller matrix ellipsometer, including e-beam patterned grating structures, nanoimprinted resist patterns, lithographic patterns with LER (line edge roughness), and etched trench nanostructures. The last sample is from the practical manufacturing process lines of

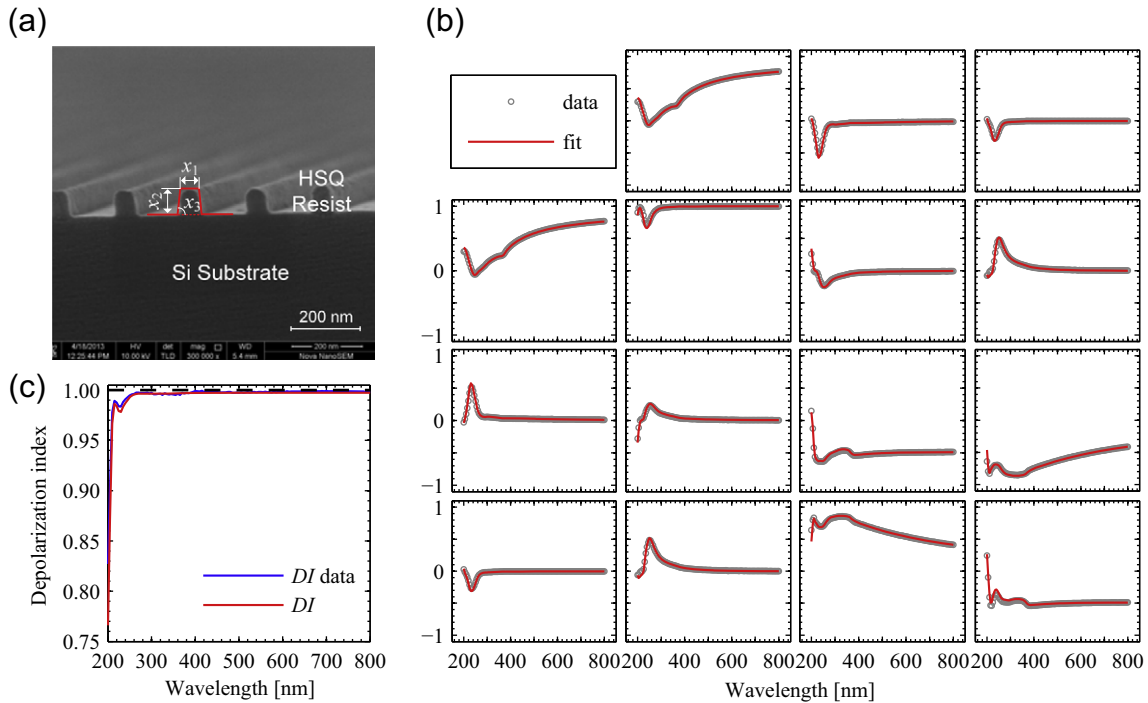


Fig. 3. (a) SEM micrograph of the investigated e-beam patterned grating structure with the applied geometric model overlaid; (b) fitting result and (c) depolarization index spectra of the measured and calculated best-fit Mueller matrix spectra when considering the depolarization effects induced by finite spectral bandwidth and NA of the ellipsometer. Data analysis was performed at the incidence angle of 65° and azimuthal angle of 60° . The spectral range was varied from 200 to 800 nm with increments of 5 nm.

Table 1

Comparison of measurands of the investigated e-beam patterned grating structure extracted from MME and SEM measurements.

Measurands	MME	SEM
x_1 (nm)	55.4 ± 0.52	56.2
x_2 (nm)	74.8 ± 0.24	72.9
x_3 (deg)	87.6 ± 0.29	86.1

flash memory storage cells, which was made on a 12 inch Si wafer that consists of thousands of dies and each die has a size of less than $280 \mu\text{m} \times 1200 \mu\text{m}$. In experiments, the spectral range was varied from 200 to 800 nm with increments of 5 nm. The incidence angle was fixed at 65° for the first three samples and was fixed at 55° for the last sample due to the small size of the dies in comparison with the spot size of instrument. The azimuthal angle was fixed at 60° for the first sample, which was achieved by performing measurement configuration optimization according to Eq. (23). As for the last three samples, the azimuthal angle was fixed at 0° to decrease RCWA calculation time, since the RCWA calculation in a conical diffraction configuration ($\phi \neq 0^\circ$) is much more time-consuming than in a planar diffraction configuration ($\phi = 0^\circ$), especially when depolarization effects are incorporated into the optical model. Although the final extracted fitting parameters from the MME measurements might not be the optimal for the last three samples in comparison with those achieved at the optimal measurement configuration, reasonable agreement between the results measured by MME and SEM/TEM measurements can still be observed. The corresponding fitting errors χ_r between the measured and calculated best-fit Mueller matrix spectra after considering depolarization effects were also presented for the four samples. As can be seen, the fits for all the four samples do not have χ_r close to 1, which is possibly attributed

to the following reasons. First, the adopted optical models are imperfect. There might be some influential structural features and unknown depolarization effects that were not incorporated into the model. Second, the estimated standard deviations of the experimental Mueller matrix elements may not reflect all of the errors in the measurement, since it has been found in our previous work [25] that the estimates of the errors in the fitting parameters usually underestimated the true errors. For this reason, the actual estimated uncertainties appended to the MME-extracted parameters were not directly obtained according to Eq. (21) but from a corrected form of Eq. (21), i.e., $u(x_i) = \kappa \times \chi_r \times \sigma(x_i)$ [25]. We will present the measurement details about the four samples in the remainder of this section.

3.1. Measurement of e-beam patterned grating structures

With the ever-downscaling in very-large scale integrated circuits, critical dimension (CD) monitoring is becoming more and more challenging. According to the International Technology Roadmap for Semiconductors (ITRS), the requirements for uncertainty in CD measurement for forth-coming process nodes are less than 2 nm [38]. The ITRS also indicates that conventional ellipsometric scatterometry is quickly reaching its limit and requires improvements for future process nodes. In this section, we try to apply MME to characterize e-beam patterned grating structures with small CDs. Fig. 3(a) depicts the SEM micrograph of the investigated e-beam patterned grating structure, which has a pitch of 180 nm and a duty cycle of 1:2, i.e., with a nominal CD of 60 nm. As shown in Fig. 3(a), we apply a symmetrical trapezoidal model with three structural parameters x_1 , x_2 and x_3 to characterize the grating line profile, where x_1 , x_2 and x_3 represent the grating width, grating height and sidewall angle, respectively. During the regression analysis, we fixed the grating pitch and just let the parameters x_1 – x_3 vary. The optical constants of the Si substrate in the rest of this section were all fixed at values taken from [39]. The optical properties of the

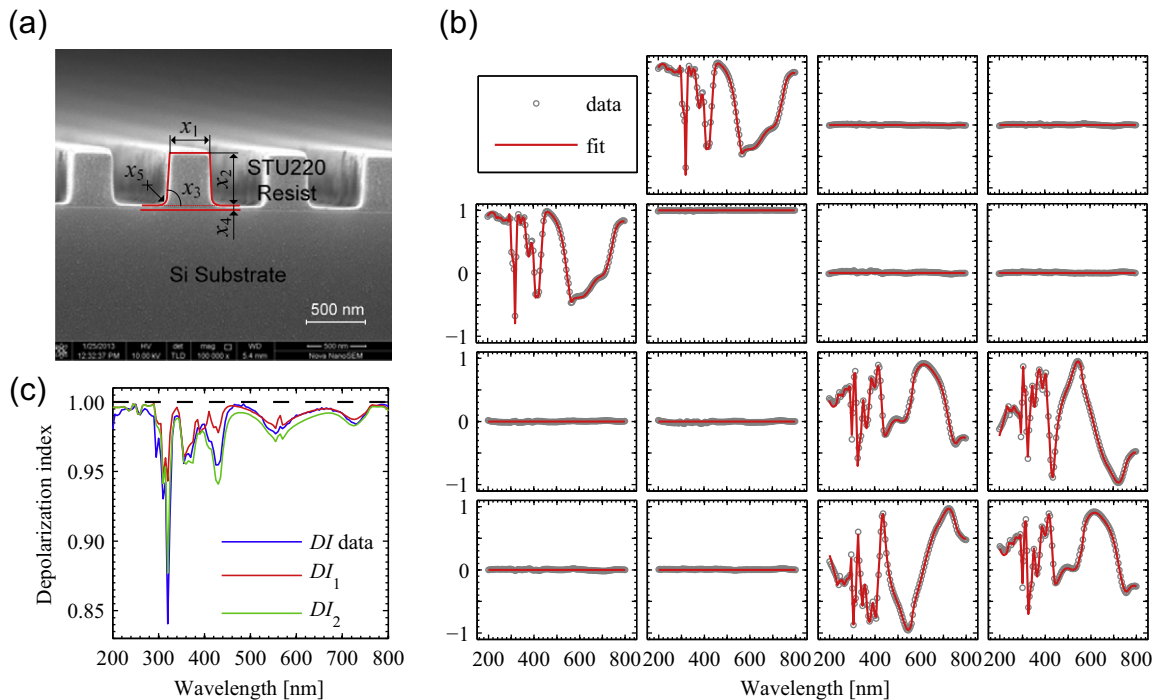


Fig. 4. (a) SEM micrograph of the investigated nanoimprinted resist pattern with the applied geometric model overlaid; (b) fitting result and (c) depolarization index spectra of the measured and calculated best-fit Mueller matrix spectra when considering the depolarization effects induced by finite spectral bandwidth and NA of the ellipsometer, as well as the residual layer thickness nonuniformity. Data analysis was performed at the incidence angle of 65° and azimuthal angle of 0° . The spectral range was varied from 200 to 800 nm with increments of 5 nm.

Table 2

Comparison of measurands of the investigated nanoimprinted resist pattern extracted from MME and SEM measurements.

Measurands	MME	SEM
x_1 (nm)	352.8 ± 0.68	352.2
x_2 (nm)	471.9 ± 0.47	472.1
x_3 (deg)	87.2 ± 0.11	87.5
x_4 (nm)	61.9 ± 0.27	57.8
x_5 (nm)	67.9 ± 2.46	–
σ_t (nm)	3.3 ± 0.31	–

hydrogen silsesquioxane (HSQ) resist were modeled using a Cauchy model modified with an Urbach tail in the extinction coefficient [34]

$$n(\lambda) = A + B/\lambda^2 + C/\lambda^4, \quad (24a)$$

$$k(\lambda) = \alpha \exp[\beta(1/\lambda - 1/\lambda_0)], \quad (24b)$$

whose parameters were determined from a HSQ resist film deposited on the Si substrate and taken as $A = 1.44$, $B = 3.78e-3 \mu\text{m}^2$, $C = 6.93e-5 \mu\text{m}^4$, $\alpha = 2.05e-4$, $\beta = 1.48 \mu\text{m}$, $\lambda_0 = 0.40 \mu\text{m}$. The wavelength λ in Eqs. (24a) and (24b) is in unit of micrometer.

Fig. 3(b) shows the ellipsometer-measured Mueller matrix spectra of the investigated e-beam patterned grating structure, and the corresponding depolarization index spectrum calculated using Eq. (8) is presented in Fig. 3(c). As can be observed from Fig. 3(c), the depolarization indices are close to 1 over most of the spectrum and show a significant dip to about ~ 0.8 near 200 nm. Considering that the ellipsometer-measured data for each recorded wavelength always contains contributions from a span of wavelengths and incident directions, we investigate the depolarization effects induced by the finite spectral bandwidth and NA of the ellipsometer. In the experiments, the instrumental spectral bandwidth and NA were pre-determined through measurements on a nominally 1000 nm SiO_2 thick thermal film on the Si substrate to isolate the effects of bandwidth and NA from sample-specific artifacts. The measurement yielded the spectral bandwidth $\sigma_\lambda = 1.0 \text{ nm}$ and

Table 3

Comparison of measurands of the investigated lithographic pattern with LER extracted from MME and SEM measurements.

Measurands	MME	SEM
x_1 (nm)	205.6 ± 1.75	198.5
x_2 (nm)	310.5 ± 0.32	308.3
x_3 (deg)	89.8 ± 0.10	89.3
x_4 (nm)	116.4 ± 0.17	115.4
x_5 (nm)	5.5 ± 0.61	4.8

$NA = 0.065$ [25]. A rectangular bandwidth function was chosen in the measurement of bandwidth. During the further regression analysis, we fixed the bandwidth and NA and let the parameters x_1 and x_2 vary. Fig. 3(b) depicts the fitting result of the measured and calculated best-fit Mueller matrix spectra when considering the depolarization effects induced by finite spectral bandwidth and NA, and Fig. 3(c) shows the depolarization index spectra associated with the measured and calculated best-fit Mueller matrix spectra. An excellent match can be observed from Fig. (3), which yields a fitting error of $\chi_r = 10.62$. Table 1 presents the comparison of fitting parameters extracted from MME and SEM measurements. The uncertainties appended to the fitting parameter values all have a 95% confidence level in the rest of this section. As observed from Table 1, the fitting parameter values extracted from MME measurements exhibit good agreement with the results measured by SEM.

3.2. Measurement of nanoimprinted resist patterns

Nanoimprint lithography (NIL), in which features on a prepatterned mold are transferred directly into a polymer material, represents a promising technique with the potential for high resolution and throughput as well as low cost. In order to control NIL processes to achieve good fidelity, accurate measurement of structural parameters of nanoimprinted patterns is highly desirable. These parameters include not only the pattern height and width but also the residual layer thickness. Fig. 4(a) depicts the SEM micrograph of the investigated nanoimprinted resist pattern,

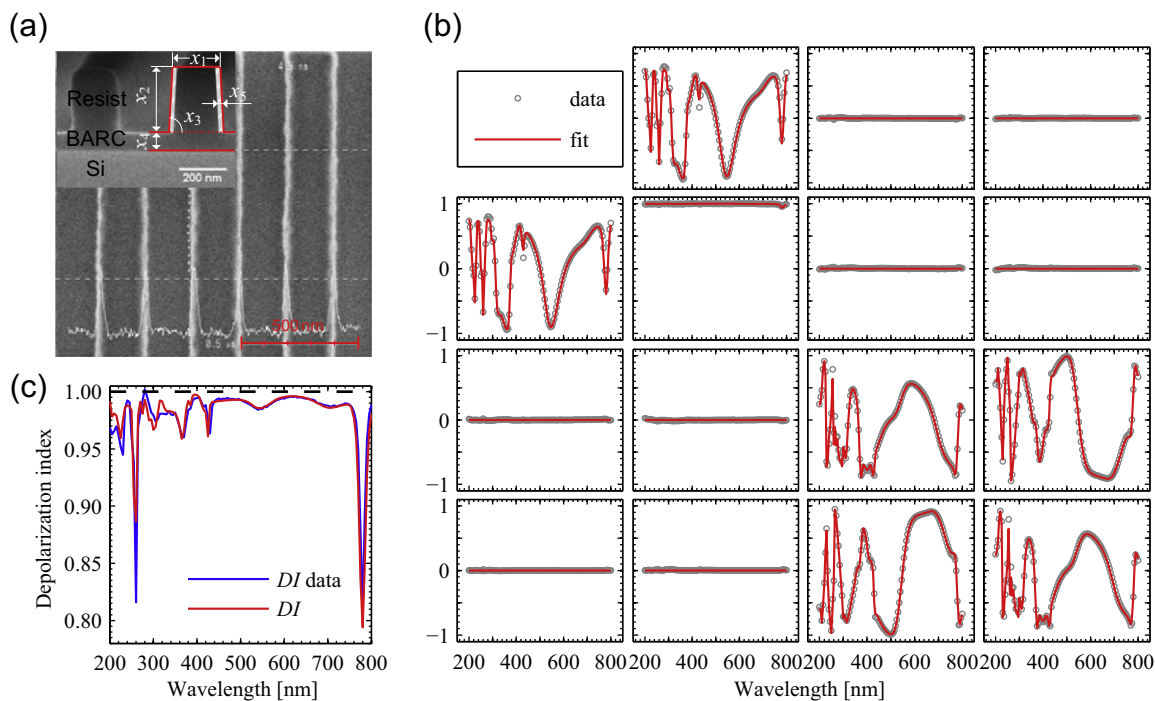


Fig. 5. (a) SEM micrograph of the investigated lithographic pattern with the applied geometric model overlaid; (b) fitting result and (c) depolarization index spectra of the measured and calculated best-fit Mueller matrix spectra when considering the depolarization effects induced by finite spectral bandwidth and NA of the ellipsometer. Data analysis was performed at the incidence angle of 65° and azimuthal angle of 0° . The spectral range was varied from 200 to 800 nm with increments of 5 nm.

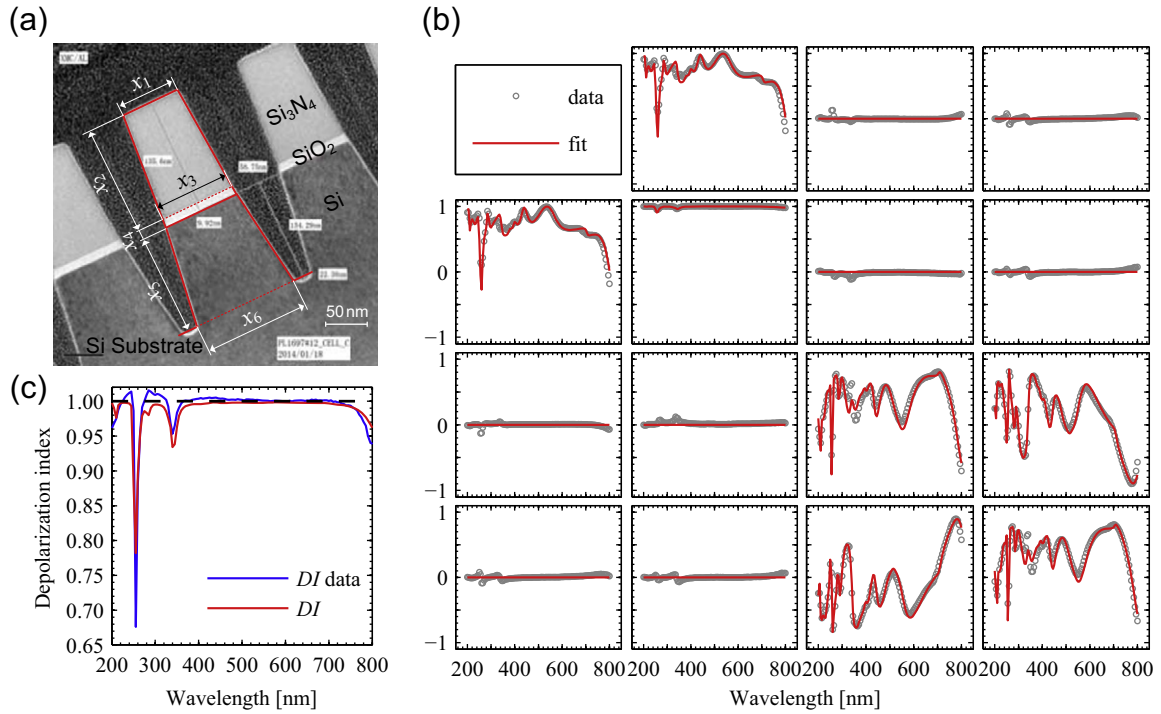


Fig. 6. (a) TEM micrograph of investigated etched trench nanostructure with the applied geometric model overlaid; (b) fitting result and (c) depolarization index spectra of the measured and calculated best-fit Mueller matrix spectra when considering the depolarization effects induced by finite spectral bandwidth and NA of the ellipsometer. Data analysis was performed at the incidence angle of 55° and azimuthal angle of 0° . The spectral range was varied from 200 to 800 nm with increments of 5 nm.

which was imprinted using a Si imprinting mold. The Si imprinting mold has gratings with a pitch of 800 nm, a top line width of 350 nm, a line height of 472 nm, and a sidewall angle of 88° [21]. As shown in Fig. 4(a), we apply a symmetrical trapezoidal model with a total of five structural parameters x_1 – x_5 to characterize the grating line profile, where x_1 , x_2 , x_3 , x_4 , and x_5 represent top line width, line height, sidewall angle, residual layer thickness, and radius of the bottom round corner, respectively. During the regression analysis, we fixed the grating pitch at 800 nm and just let the parameters x_1 – x_5 vary. The optical properties of the STU220 resist were modeled using a two-term Forouhi–Bloomer model [40], whose parameters were determined from a STU220 resist film deposited on the Si substrate and taken as $A_1 = 4.447e-3$, $A_2 = 3.051e-2$, $B_1 = 8.8611$ eV, $B_2 = 12.0043$ eV, $C_1 = 19.6703$ eV², $C_2 = 36.3258$ eV², $n(\infty) = 1.4842$, and $E_g = 3.3724$ eV.

Fig. 4(b) shows the ellipsometer-measured Mueller matrix spectra of the investigated nanoimprinted resist pattern, and the corresponding depolarization index spectrum is presented in Fig. 4(c). As can be observed from Fig. 4(c), the depolarization indices are close to 1 over most of the spectrum except for the range from ~ 300 to 460 nm and show significant dips to ~ 0.84 near 320 nm. Clearly, the investigated nanoimprinted grating structure exhibits noticeable depolarization effects that should be included in the interpretation of the ellipsometer-measured data. As did in Section 3.1, we first incorporated the depolarization effects induced by the instrumental finite spectral bandwidth and NA

into the optical model. The depolarization index spectrum DI_1 corresponding to the achieved best-fit calculated Mueller matrix spectra is presented in Fig. 4(c). As shown in Fig. 4(c), the measured and calculated depolarization indices show good agreement with the spectral range from ~ 460 to 800 nm, but exhibit poor performance within the spectral range from ~ 300 to 460 nm. We then further took the depolarization effect induced by residual layer thickness nonuniformity into account. During the further regression analysis, we let the parameters x_1 – x_5 as well as the standard deviation σ_r of the residual layer thickness vary. The depolarization index spectrum DI_2 shown in Fig. 4(c) corresponds to the calculated best-fit Mueller matrix spectra when further considering the depolarization effect induced by residual layer thickness nonuniformity. As shown in Fig. 4(c), the match between the measured and calculated depolarization index spectra is significantly improved, especially in the spectral range from ~ 300 to 460 nm. Fig. 4(b) depicts the fitting result between the measured and calculated best-fit Mueller matrix spectra when taking the depolarization effects induced by instrumental finite spectral bandwidth and NA as well as residual layer thickness nonuniformity into account, which yields a fitting error of $\chi_r = 5.31$. Table 2 presents the corresponding MME-extracted parameter values and SEM measurement results. As observed from Table 2, the MME-extracted parameter values are in excellent agreement with the results measured by SEM. In addition, the MME-extracted parameter values of the nanoimprinted resist pattern are also in good agreement with the Si imprinting mold. It therefore indicates an excellent fidelity of the nanoimprint pattern transfer process.

Table 4

Comparison of measurands of the investigated etched trench nanostructure extracted from MME and TEM measurements.

Measurands	MME	TEM
x_1 (nm)	74.1 ± 0.40	75.0
x_2 (nm)	133.9 ± 0.59	135.6
x_3 (nm)	89.9 ± 0.31	86.9
x_4 (nm)	14.0 ± 0.70	9.9
x_5 (nm)	134.0 ± 0.53	134.3
x_6 (nm)	125.6 ± 0.30	129.6

3.3. Measurement of lithographic patterns with line edge roughness

With the gate dimensions of transistors shrinking to the decanometer regime, the impact of line roughness on performances of microelectronic devices has become a more and more non-ignorable issue in semiconductor manufacturing. In-line line roughness monitoring is of great importance, and it is extremely desirable if the metrology technique is fast, inexpensive, nondestructive and reliable. In this section, we try to apply MME to characterize lithographic patterns with LER. Fig. 5(a)

depicts the SEM micrograph of the investigated lithographic pattern overlaid with the applied geometric model, which has a pitch of 400 nm. As shown in Fig. 5(a), the photoresist grating is characterized by top critical dimension x_1 , grating height x_2 , and sidewall angle x_3 . The thickness of the bottom anti-reflective coating (BARC) is represented by x_4 . The rough edges of grating lines were approximated as effective medium boundary layers with thickness x_5 . This approximation simplifies the rough grating to a one-dimensional (1D) periodic structure. We can then perform simulations using a 1D RCWA solution. During the regression analysis, we fixed the grating pitch and just let the parameters x_1 – x_5 vary. The optical properties of the BARC layer were modeled using a two-term Forouhi–Bloomer model [40], whose parameters were determined from a BARC film deposited on the Si substrate and taken as $A_1 = 6.029e-3$, $A_2 = 2.060e-2$, $B_1 = 14.1953$ eV, $B_2 = 14.1964$ eV, $C_1 = 50.5239$ eV², $C_2 = 50.5379$ eV², $n(\infty) = 1.4361$, and $E_g = 4.7741$ eV. The optical properties of the photoresist were modeled using a Tauc–Lorentz model [41], whose parameters were also determined from a photoresist film deposited on the Si substrate and taken as $\epsilon_\infty = 1.4268$, $E_g = 3.4597$ eV, $A = 21.1496$ eV, $C = 0.9877$ eV, and $E_0 = 9.9492$ eV. Fig. 5(b) shows the fitting result of the ellipsometer-measured and calculated best-fit Mueller matrix spectra when considering the depolarization effects induced by finite spectral bandwidth and NA, and Fig. 5(c) shows the depolarization index spectra associated with the measured and calculated best-fit Mueller matrix spectra. The fit shown in Fig. 5(b) yields a fitting error of $\chi_r = 13.74$. Table 3 presents the comparison of fitting parameters extracted from MME and SEM measurements. As can be observed from Table 3, the MME-extracted parameters exhibit good agreement with the results measured by SEM, which therefore demonstrates the potential of MME in line roughness metrology.

3.4. Measurement of etched trench nanostructures

Flash memory is an electronic non-volatile computer storage medium that can be electrically erased/reprogrammed. Due to the much lower cost than byte-programmable EEPROM (electrically erasable programmable read-only memory), flash memory has become the dominant memory type wherever a system requires a significant amount of non-volatile, solid state storage. The key of flash memory is its storage cells, which are usually comprised of some nanostructures. Accurate characterization of geometrical profiles of these nanostructures is of great importance. Fig. 6(a) depicts the TEM micrograph of the investigated etched trench nanostructure overlaid with the applied geometric model, which is usually encountered in the manufacturing of flash memory storage cells. The pitch of the etched trench nanostructure is 154 nm. As shown in Fig. 6(a), the etched trench nanostructure has three grating layers. The Si₃N₄ grating layer is characterized by top critical dimension x_1 , grating height x_2 , and bottom critical dimension x_3 . The SiO₂ grating layer has the same sidewall angle with that of the Si₃N₄ grating layer and is characterized by top critical dimension x_3 and grating height x_4 . The Si grating layer has a different sidewall angle to that of the former two grating layers and is characterized by grating height x_5 and bottom critical dimension x_6 . During the regression analysis, we fixed the grating pitch and just let the parameters x_1 – x_6 vary. The optical constants of Si₃N₄ and SiO₂ were fixed at values taken from [42]. Fig. 6(b) shows the fitting result of the ellipsometer-measured and calculated best-fit Mueller matrix spectra when considering the depolarization effects induced by finite spectral bandwidth and NA, and Fig. 6(c) shows the depolarization index spectra associated with the measured and calculated best-fit Mueller matrix spectra. The fit shown in Fig. 6(b) yields a fitting error of $\chi_r = 18.46$. Table 4 presents the comparison of fitting parameters extracted from MME and TEM measurements. As can be observed, Fig. 6(c) exhibits a good match between the measured and calculated Mueller matrix spectra, and Table 4 shows the excellent agreement between the MME-extracted and TEM-measured results.

4. Conclusions

In summary, we have presented the basic principles and instrumentation of MME, with a demonstration of the development of a broadband dual rotating-compensator Mueller matrix ellipsometer in our lab. According to the fundamental concept of computational metrology, we point out that the MME-based nanostructure metrology is essentially a computational metrology technique by modeling a complicated forward process followed by solving a corresponding inverse problem. We have applied MME to measure several typical nanostructures, including the e-beam patterned grating structures, nanoimprinted resist patterns, lithographic patterns with LER, and etched trench nanostructures that are usually encountered in flash memory process lines. These case studies have demonstrated the capability of MME in nanostructure metrology. It is expected that MME will provide a powerful tool for nanostructure metrology in future high-volume manufacturing.

Acknowledgments

This work was funded by the National Natural Science Foundation of China (grant nos. 51475191 and 51405172), the National Instrument Development Specific Project of China (grant no. 2011YQ160002), the China Postdoctoral Science Foundation (grant no. 2014M560607), and the Program for Changjiang Scholars and Innovative Research Team in University of China (grant no. IRT13017). The authors would like to thank Dr. Yasin Ekinici and Dr. Li Wang at Paul Scherrer Institute (5232 Villigen PSI, Switzerland), Dr. Fan Wang and Dr. Hailiang Lu at Shanghai Micro Electronics Equipment Co., Ltd. (Shanghai, China), and Dr. Zhimou Xu and Mr. Zhichao Ma at Huazhong University of Science and Technology (Wuhan, China) for preparing the samples and taking the SEM images.

References

- [1] M.T. Postek, K.W. Lyons, Instrumentation, metrology, and standards: key elements for the future of nanomanufacturing, *Proc. SPIE* 6648 (2007) 664802.
- [2] R.M.A. Azzam, N.M. Bashara, *Ellipsometry and Polarized Light*, North-Holland, Netherland, 1977.
- [3] X. Niu, N. Jakatdar, J. Bao, C. Spanos, Specular spectroscopic scatterometry, *IEEE Trans. Semicond. Manuf.* 14 (2001) 97.
- [4] H.T. Huang, W. Kong, F.L. Terry Jr., Normal-incidence spectroscopic ellipsometry for critical dimension monitoring, *Appl. Phys. Lett.* 78 (2001) 3893.
- [5] H.T. Huang, F.L. Terry Jr., Spectroscopic ellipsometry and reflectometry from gratings (scatterometry) for critical dimension measurement and in situ, real-time process monitoring, *Thin Solid Films* 455 (2004) 828.
- [6] H.J. Patrick, T.A. Germer, Y.F. Ding, H.W. Ro, L.J. Richter, C.L. Soles, Scatterometry for in situ measurement of pattern flow in nanoimprinted polymers, *Appl. Phys. Lett.* 93 (2008) 233105.
- [7] M.G. Faruk, S. Zangoie, M. Angyal, D.K. Watts, M. Sendelbach, L. Economikos, P. Herrera, R. Wilkins, Enabling scatterometry as an in-line measurement technique for 32 nm BEOL application, *IEEE Trans. Semicond. Manuf.* 24 (2011) 499.
- [8] A.C. Diebold, *Handbook of Silicon Semiconductor Metrology*, CRC Press, New York, 2001. (chap. 18).
- [9] C.J. Raymond, Overview of scatterometry applications in high volume silicon manufacturing, *AIP Conf. Proc.* 788 (2005) 394.
- [10] C.W. Zhang, S.Y. Liu, T.L. Shi, Z.R. Tang, Improved model-based infrared reflectometry for measuring deep trench structures, *J. Opt. Soc. Am. A* 26 (2009) 2327.
- [11] J.L. Zhu, S.Y. Liu, X.G. Chen, C.W. Zhang, H. Jiang, Robust solution to the inverse problem in optical scatterometry, *Opt. Express* 22 (2014) 22031.
- [12] X.G. Chen, S.Y. Liu, C.W. Zhang, J.L. Zhu, Improved measurement accuracy in optical scatterometry using fitting error interpolation based library search, *Measurement* 46 (2013) 2638.
- [13] X.G. Chen, S.Y. Liu, C.W. Zhang, H. Jiang, Improved measurement accuracy in optical scatterometry using correction-based library search, *Appl. Opt.* 52 (2013) 6726.
- [14] J.L. Zhu, S.Y. Liu, C.W. Zhang, X.G. Chen, Z.Q. Dong, Identification and reconstruction of diffraction structures in optical scatterometry using support vector machine method, *J. Micro/Nanolith. MEMS MOEMS* 12 (2013) 012004.
- [15] P.L. Jiang, H. Chu, J. Hench, D. Wack, Forward solve algorithms for optical critical dimension metrology, *Proc. SPIE* 6922 (2008) 692210.
- [16] M.G. Moharam, E.B. Grann, D.A. Pommet, T.K. Gaylord, Formulation for stable and efficient implementation of the rigorous coupled-wave analysis of binary gratings, *J. Opt. Soc. Am. A* 12 (1995) 1068.
- [17] L. Li, New formulation of the Fourier modal method for crossed surface-relief gratings, *J. Opt. Soc. Am. A* 14 (1997) 2758.

- [18] S.Y. Liu, Y. Ma, X.G. Chen, C.W. Zhang, Estimation of the convergence order of rigorous coupled-wave analysis for binary gratings in optical critical dimension metrology, *Opt. Eng.* 51 (2012) 081504.
- [19] T. Novikova, A. De Martino, S.B. Hatit, B. Drévilion, Application of Mueller polarimetry in conical diffraction for critical dimension measurements in microelectronics, *Appl. Opt.* 45 (2006) 3688.
- [20] T. Novikova, A. De Martino, P. Bulkin, Q. Nguyen, B. Drévilion, V. Popov, A. Chumakov, Metrology of replicated diffractive optics with Mueller polarimetry in conical diffraction, *Opt. Express* 15 (2007) 2033.
- [21] X.G. Chen, S.Y. Liu, C.W. Zhang, H. Jiang, Measurement configuration optimization for accurate grating reconstruction by Mueller matrix polarimetry, *J. Micro/Nanolith. MEMS MOEMS* 12 (2013) 033013.
- [22] Y.N. Kim, J.S. Paek, S. Rabello, S. Lee, J. Hu, Z. Liu, Y. Hao, W. McGahan, Device based in-chip critical dimension and overlay metrology, *Opt. Express* 17 (2009) 21336.
- [23] J. Li, J.J. Hwu, Y. Liu, S. Rabello, Z. Liu, J. Hu, Mueller matrix measurement of asymmetric gratings, *J. Micro/Nanolith. MEMS MOEMS* 9 (2010) 041305.
- [24] X.G. Chen, C.W. Zhang, S.Y. Liu, Depolarization effects from nanoimprinted grating structures as measured by Mueller matrix polarimetry, *Appl. Phys. Lett.* 103 (2013) 151605.
- [25] X.G. Chen, S.Y. Liu, C.W. Zhang, H. Jiang, Z.C. Ma, T.Y. Sun, Z.M. Xu, Accurate characterization of nanoimprinted resist patterns using Mueller matrix ellipsometry, *Opt. Express* 22 (2014) 15165.
- [26] S.Y. Liu, Computational metrology for nanomanufacturing, *Proc. SPIE* 8916 (2013) 891606.
- [27] S.Y. Liu, X.G. Chen, C.W. Zhang, Mueller matrix polarimetry: a powerful tool for nanostructure metrology, *ECS Trans.* 60 (2014) 237.
- [28] M. Bass, *Handbook of Optics*, third ed. McGraw-Hill, New York, 2010. (vol. 1, chap. 15).
- [29] A. De Martino, Y.K. Kim, E. Garcia-Caurel, B. Larde, B. Drévilion, Optimized Mueller polarimeter with liquid crystals, *Opt. Lett.* 28 (2003) 616.
- [30] E. Garcia-Caurel, A. De Martino, B. Drévilion, Spectroscopic Mueller polarimeter based on liquid crystal devices, *Thin Solid Films* 455–456 (2004) 120.
- [31] R.M.A. Azzam, Photopolarimeter measurement of the Mueller matrix by Fourier analysis of a single detected signal, *Opt. Lett.* 2 (1978) 148.
- [32] R.W. Collins, J. Koh, Dual rotating-compensator multichannel ellipsometer: instrument design for real-time Mueller matrix spectroscopy of surfaces and films, *J. Opt. Soc. Am. A* 16 (1999) 1997.
- [33] O. Arteaga, J. Freudenthal, B. Wang, B. Kahr, Mueller matrix polarimetry with four photoelastic modulators: theory and calibration, *Appl. Opt.* 51 (2012) 6805.
- [34] H. Fujiwara, *Spectroscopic Ellipsometry Principles and Applications*, Wiley, West Sussex, 2007.
- [35] J.J. Gil, E. Bernabeu, Depolarization and polarization indices of an optical system, *Opt. Acta (Lond.)* 33 (1986) 185.
- [36] H.C. van de Hulst, *Light Scattering by Small Particles*, Dover, New York, 1981.
- [37] X.G. Chen, S.Y. Liu, H.G. Gu, C.W. Zhang, Formulation of error propagation and estimation in grating reconstruction by a dual-rotating compensator Mueller matrix polarimeter, *Thin Solid Films* 571 (2014) 653.
- [38] ITRS report, 2013 ed. <http://public.itrs.net>.
- [39] C.H. Herzinger, B. Johs, W.A. McGahan, J.A. Woollam, W. Paulson, Ellipsometric determination of optical constants for silicon and thermally grown silicon dioxide via a multi-sample, multi-wavelength, multi-angle investigation, *J. Appl. Phys.* 83 (1998) 3323.
- [40] A.R. Forouhi, I. Bloomer, Optical properties of crystalline semiconductors and dielectrics, *Phys. Rev. B* 38 (1988) 1865.
- [41] G.E. Jellison Jr., F.A. Modine, Parameterization of the optical functions of amorphous materials in the interband region, *Appl. Phys. Lett.* 69 (1996) 371.
- [42] E.D. Palik, *Handbook of Optical Constant of Solids*, Academic Press, San Diego, 1991.